PAPER

Check for updates

An artificial hybrid interphase for an ultrahigh-rate and practical lithium metal anode†

Anjun Hu, ‡[a] Wei Chen,‡[a] Xinchuan Du,‡[a] Yin Hu,[ab] Tianyu Lei,[a] Hongbo Wang,[a] Lanxin Xue,[a] Yaoyao Li,[a] He Sun,[a] Yichao Yan,[a] Jianping Long,[c] Chaozhu Shu,[c] Jun Zhu,[a] Baihai Li, *[b] Xianfu Wang *[a] and Jie Xiong *[a]

The solid electrolyte interphase (SEI) layer is pivotal for stable lithium (Li) metal batteries especially under a high rate. However, the mechanism of Li$^+$ transport through the SEI has not been clearly elucidated to build robust Li anodes for practical Li metal batteries. Herein, an artificial hybrid SEI layer consisting of lithium-antimony (Li$_3$Sb) alloy and lithium fluoride (LiF) is constructed to explore the ion diffusion behaviors within the SEI. As evidenced theoretically and experimentally, Li$_3$Sb is identified as a superionic conductor for Li$^+$ transport and as an interfacial stabilizer for the SEI layer while the LiF component with superior electron-blocking capability reduces the electron tunneling from the Li anode into the SEI, resulting in uniform dendrite-free Li deposition at the SEI/Li interface and stable Li plating/stripping behaviors at an ultrahigh rate of 20 mA cm^{-2}. A practical 325.28 W h kg^{-1} pouch cell is well demonstrated under a high sulfur loading of 6 mg cm^{-2} and a low electrolyte/sulfur ratio of 3 μl mg^{-1}. This work uncovers the internal mechanism of Li$^+$ transport within the SEI component, and provides an avenue to stabilize the Li anode under practical high-rate conditions.

Broader context

Lithium (Li) metal offers the lowest electrode potential and an ultrahigh theoretical specific capacity for energy storage. However, its practical application under a high rate is hampered by the limited Li$^+$ transport through the solid electrolyte interphase (SEI). Moreover, the elucidation of the SEI as a Li$^+$ transport medium and the role of the SEI component in the ion diffusion behaviors are not well established yet. Here we aim to fill this gap by providing an insight into the internal mechanism of Li$^+$ transport within the SEI theoretically and experimentally based on a hybrid Li$_3$Sb/LiF-based SEI. Li$_3$Sb is identified as a fast Li$^+$ transport medium and interfacial stabilizer for the SEI layer while LiF with superior electron-blocking capability reduces the electron tunneling from the anode into the SEI. Benefiting from these merits, the hybrid SEI modified Li anode enables uniform Li deposition at the SEI/Li interface and stable Li plating/stripping behavior under an ultrahigh rate. The practical demonstration of a 0.4 A h-level Li–S pouch cell is achieved by the modified Li anode at high sulfur loading and lean electrolyte conditions. These results, in addition to revealing the diffusion mechanism of Li$^+$ in the SEI, are a step forward to stabilize the Li anode under practical high-rate conditions.

Introduction

Lithium metal batteries (LMBs) are actively developed as a next generation electric storage device owing to the high theoretical specific capacity (3860 mA h g^{-1}), light weight (0.534 g cm^{-3}), and the lowest negative electrochemical potential (−3.04 V *vs.*

standard hydrogen electrode) of the Li metal.[1–3] In practical operation, because of the lower electrochemical potential of Li than that of the electrolytes, spontaneous reactions of the Li metal with organic components in the electrolytes occur and form a solid electrolyte interphase (SEI) on the Li surface,[4,5] whose properties can strongly impact the Li plating/stripping behavior that largely determines the practical implementation of LMBs.[6,7]

In general, Li deposition can occur within the SEI or at the SEI/Li interface, which depends on two competing processes (the Li$^+$ diffusion rate from the SEI to the Li anode and the electron tunneling capability from the anode into the SEI).[8] Assuming that the SEI exhibits sufficient insulativity to prevent electron transfer from the Li anode into the SEI, and the Li$^+$ transport in the SEI is fast enough, the Li metal tends to be

[a] *State Key Laboratory of Electronic Thin Film and Integrated Devices, University of Electronic Science and Technology of China, Chengdu, 610054, China. E-mail: xfwang87@uestc.edu.cn, jiexiong@uestc.edu.cn*

[b] *School of Materials and Energy, University of Electronic Science and Technology of China, Chengdu 610054, China. E-mail: libaihai@uestc.edu.cn*

[c] *College of Materials and Chemistry & Chemical Engineering, Chengdu University of Technology, Chengdu 610059, China*

† Electronic supplementary information (ESI) available. See DOI: 10.1039/d1ee00508a
‡ These authors contributed equally to this work.

This journal is © The Royal Society of Chemistry 2021

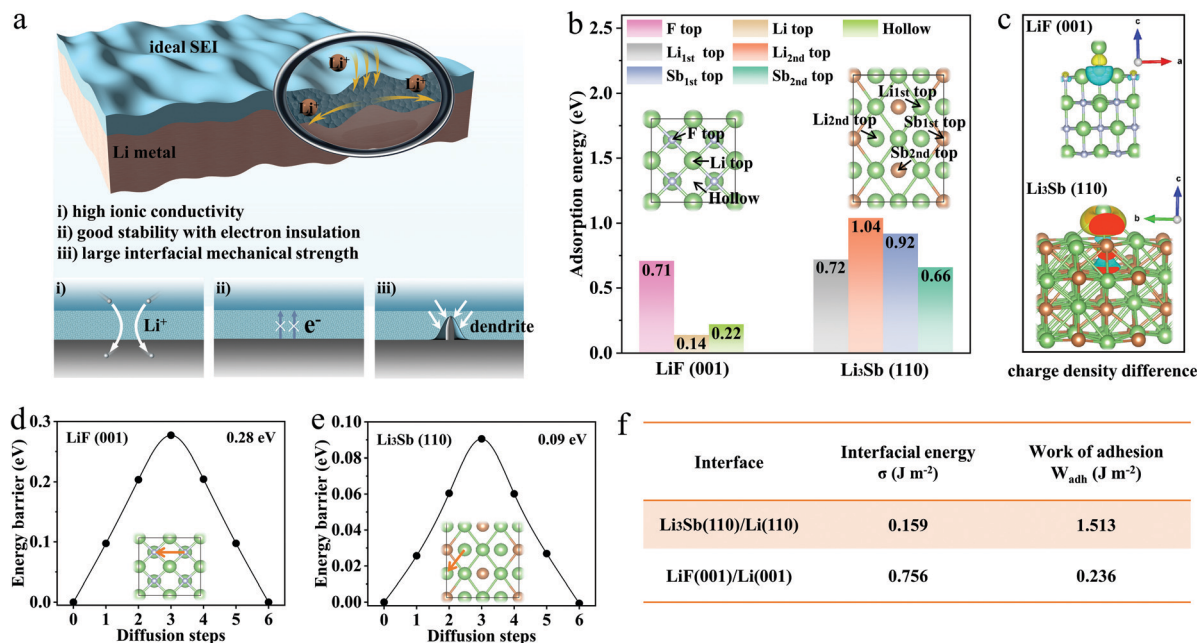*Energy Environ. Sci.,* 2021, **14**, 4115–4124 | **4115**

Fig. 1 Design concept of an artificial hybrid interphase. (a) Schematic illustration of an ideal SEI. (b) Adsorption sites and the corresponding adsorption energy of for Li$^+$ on the LiF(001) and Li$_3$Sb(110) surfaces. The inset is the top-view of the adsorption sites for Li$^+$ on the 2 × 2 LiF(001) (left) and 1 × 2 Li$_3$Sb(110) (right) surfaces. The outmost atoms were connected with bonds. (c) Charge density differences of Li$^+$ on the surfaces of LiF(001) and Li$_3$Sb(110). The yellow and cyan spheres represent electron accumulation and depletion, respectively. The isosurface level is 0.002 e Å^{-3}. Kinetic energy barriers of Li$^+$ diffusion on the (d) LiF(001) and (e) Li$_3$Sb(110) surfaces. The orange arrows represent the diffusion pathways on the surfaces. (f) The calculated interfacial energy (σ) and the work of adhesion (W_{adh}) for the interfacial supercells.

deposited at the SEI/Li interface; otherwise, it may form a nucleus inside the SEI layer. The latter case is far worse especially under high current density because these nuclei completely lose electronic contact with the anode and thus trigger uneven Li deposition due to the local electrical field distribution.[8] Furthermore, these isolated Li dendrites within the SEI can also potentially break the SEI layer, which causes more parasitic reactions between the fresh Li anode and the electrolyte.[9,10] Therefore, to mitigate Li plating within the SEI, high ionic conductivity and electronic insulative properties are two primary features for an ideal SEI layer. In addition, the high interfacial mechanical strength is also vital to bear the huge volume change and inhibit the dendritic growth at the SEI/Li metal interface (Fig. 1a).[11–13]

These critical features of the SEI layer are primarily determined by its chemical composition and structure. It is well established that the SEI layer consists of an inorganic inner layer and an organic outer layer.[14] Three main inorganic components (LiF, Li$_2$CO$_3$, and Li$_2$O) constitute the dense layer of the SEI that tightly adhere to the Li anode. Among the components, LiF provides the highest electron tunneling barrier and excellent mechanical strength.[9,15] Therefore, the increase of LiF can reduce the electron tunneling probability at the SEI/Li interface and thus prevent the penetration of undesirable Li dendrites into the SEI.[16] However, the high ion migration barrier of LiF worsens the diffusion kinetics of Li$^+$ through the SEI, which leads to large Li plating/stripping overpotentials especially under a high rate.[17] Although considerable efforts have been dedicated to regulating the Li$^+$ diffusion kinetics by engineering the composition[18,19] and structural homogeneity[20,21] of the SEI as well as to understanding the

formation/growth mechanisms of the SEI,[9,22] the elucidation of the SEI as a Li$^+$ transport medium and the role of the SEI component in the ion diffusion behaviors are not well established yet. Therefore, to achieve a stable Li metal anode under practical high-rate conditions, it is pivotal to understand the internal mechanism of Li$^+$ transport within the SEI theoretically and experimentally.

Inspired by the superionic behavior of the lithium-antimony (Li$_3$Sb) alloy (Li$^+$ diffusion coefficient is 2.0 × 10^{-4} cm^2 s^{-1}, Table S1, ESI†), herein, an artificial hybrid SEI is constructed by incorporating the Li$_3$Sb component with LiF to study the mechanism of Li$^+$ transport in the SEI layer. The Li$_3$Sb component as an ionic channel eliminates Li$^+$ diffusion barriers within the interphase layer while the electronically insulating LiF can serve as a blocking shield of electrons at the SEI/Li interface, achieving uniform Li deposition at the SEI/Li interface. In addition, since the hybrid interphase inherits robust interfacial mechanical stability, the dendrite growth is effectively suppressed. As a result, the symmetric cell with the modified Li anode achieves an extended Li plating/stripping stability over 1360 cycles with a much reduced voltage polarization (100 mV) at a rate of 20 mA cm^{-2}. For practical demonstration, by pairing with the modified Li anode, the assembled 0.4 A h Li–S pouch cell can achieve a high specific energy density of 325.28 W h kg^{-1} with a capacity retention of 91.5% after 60 cycles under a high sulfur loading of 6 mg cm^{-2} and a low electrolyte/sulfur ratio of 3 μl mg^{-1}. This effective strategy and the corresponding revelation of the inherent mechanism hold enormous promise for developing high-energy and long-life Li metal batteries.

Results and discussion

Design principles of an artificial hybrid interphase

The benefit of an artificial hybrid interphase was corroborated *via* density functional theory (DFT) calculations. The surface models of $Li_3Sb(110)$ and $LiF(001)$, which have the lowest surface energies (Fig. S1, S2, Table S2 and Note S1a, ESI†), were established as the substrates for investigating the adsorption and migration kinetics of Li^+ (Note S1b, ESI†). As shown in Fig. 1b and Table S3 (ESI†), four possible sites on the $Li_3Sb(110)$ surface were considered for Li^+ adsorption. The Li_{2nd}-top site is identified as the most stable position for the adsorbed Li^+ with an adsorption energy of 1.04 eV. The $LiF(001)$ surface is less complicated, where three candidate positions allow adsorption of Li^+. The F-top site is the most stable position for Li^+ with an adsorption energy of 0.71 eV. Li_3Sb exhibits relatively large adsorption energies compared to LiF, indicating that Li_3Sb has higher affinity towards Li^+. Meanwhile, the charge density differences visualized in Fig. 1c evidence the stronger interfacial interactions of Li^+ with the $Li_3Sb(110)$ surface than with the $LiF(001)$ surface. Bader charge analysis[23] indicates that 0.12 electrons transfer from Li^+ to the coordinated atoms of the $Li_3Sb(110)$ surface, which is much higher than that occurring at the Li/LiF interface (0.04 electrons). Moreover, the diffusion of Li^+ between the most stable adsorption sites was investigated *via* the climbing-image nudged elastic band (CI-NEB) method and is shown with the energy profiles in Fig. 1d and e. As a result, the energy barriers of Li^+ diffusion on the $Li_3Sb(110)$ and $LiF(001)$ surfaces are 0.09 eV and 0.28 eV, respectively, which are lower than that of the Li(001) surface (0.39 eV).[24] Therefore, it can be concluded that the stronger adsorption of $Li_3Sb(110)$ towards Li^+ can concentrate Li^+ preferentially on its surface, and the lower diffusion energy of Li^+ then allows the rapid transport of Li^+ through the SEI layer.

As a further step, to theoretically evaluate the effect of Li_3Sb and LiF on suppression of the Li dendrites, supercells with incoherent sharp interfaces were constructed based on the interfacial misfit minimization (Fig. S3 and Note S1c, ESI†). Then interfacial properties, including the formation energy (E_f), strain energy (ζ), interfacial energy (σ) and the work of adhesion (W_{adh}) of the artificial SEI/Li interface, were calculated for mechanical stability evaluation,[8,25] which are tabulated in Fig. 1f and Table S4 (ESI†). The results of σ and W_{adh} were employed to evaluate the interface mechanical stability and a higher W_{adh} corresponds to better interfacial strength. The calculated results show that the Li_3Sb/Li interface exhibits a higher W_{adh} (1.513 J m^{-2}) and a lower σ (0.159 J m^{-2}) compared to those of the LiF/Li interface, respectively, indicating that the former interface is more stable.

These results show that the incorporation of the Li_3Sb component into the LiF-rich SEI layer is expected to achieve enhanced Li^+ adsorption and diffusion properties and a stabilized Li metal anode.

Construction of the artificial hybrid interphase

The artificial hybrid interphase layer was constructed on the Li metal surface by immersing the Li metal in an aprotic dimethyl ether (DME) solvent containing antimony trifluoride (SbF_3) at room temperature (Fig. 2a and Fig. S4, ESI†). One key feature of the preparation strategy is that the low-cost SbF_3 precursor is used as a competitive substitute, compared with recently reported metal halides (Table S5, ESI†). The SbF_3 undergoes a displacement reaction with the Li metal, leading to the formation of LiF and Sb products. The displaced Sb products then react with the underlying Li metal and the reaction proceeds until a single phase composition (Li_3Sb) is achieved. The treatment processes are also fast and thermodynamically spontaneous due to the large electronegativity difference between metallic Li and Sb.[26] Moreover, the phase diagram of the Li–Sb–F system further confirms the thermodynamically stable phase of Li_3Sb and LiF (Fig. S5, ESI†). Meanwhile, a porous and ion-conducting SEI layer (such as Li_2CO_3, LiOH, Li_2O, *etc.*) will form naturally when the Li metal is immersed in an aprotic DME solvent.[27] With the increasing concentration of SbF_3, the Li surface after treatment ranges from dark brown to dark black (Fig. S6, ESI†); the interphase layer formed is represented as LiF/Li_3Sb-x (x = 1, 5, 10, and 50, respectively, representing the molar concentration of SbF_3).

The morphological and structural features of the artificial hybrid interphase can be obtained from scanning electron microscopy (SEM). The LiF/Li_3Sb-5 layer shows a dense surface covered with spherical aggregates (Fig. 2b and c) and the thickness is estimated to be 5 µm (Fig. 2d). Energy dispersive spectroscopy (EDS) mapping and three-dimensional (3D) reconstruction of the interphase layer show even distribution of Li, Sb, and F elements (Fig. 2e and Fig. S7, ESI†), which is conducive to establish uniform distribution of the electric field and ion concentration for facilitating homogeneous Li^+ diffusion through the SEI.[28] In addition, the compact surface morphology of LiF and Li_3Sb contributes to the surface mechanical strength, which is expected to withstand the volume change and provide sufficient mechanical stability for inhibiting the growth of Li dendrites.[29] Moreover, the optimal thickness of the hybrid LiF/Li_3Sb-5 interphase layer was found to be 5 µm (Fig. S8 and Note S2, ESI†), because of the limited Li^+ transport in the thicker interphase layer and the poor suppression ability of the thinner layer against dendritic growth. This was further verified by Li plating/stripping measurements and electrochemical impedance spectroscopy (EIS). The LiF/Li_3Sb-5 symmetric cell achieves the longest Li plating/stripping stability over 1100 h at 2 mA cm^{-2} (2 mA h cm^{-2}) (Fig. S9, ESI†). In addition, the LiF/Li_3Sb-5 exhibits the lowest charge transfer resistance (R_{ct}) value of 67.1 Ω (Fig. S10, Note S3 and Table S6, ESI†). Therefore, the artificial hybrid interphase layer with moderate thickness (5 µm) stabilizes the Li interface, and the modified Li anode exhibits minimal interfacial resistance and superior cycling stability.

The components of the equilibrated artificial hybrid interphase were analyzed by X-ray diffraction (XRD) and Raman spectra (Fig. 2f and Fig. S11, Note S4, ESI†), showing that Li_3Sb and LiF are the crystalline phases in the Li-rich hybrid interphase on the Li foils. In addition, the chemical compositions of the interphase were investigated *via* X-ray photoelectron spectroscopy (XPS) with Ar^+ sputtering (Fig. 2g and Note S5, ESI†) and time-of-flight secondary ion mass spectrometry (TOF-SIMS) (Fig. S12, S13 and Note S6, ESI†).

This journal is © The Royal Society of Chemistry 2021

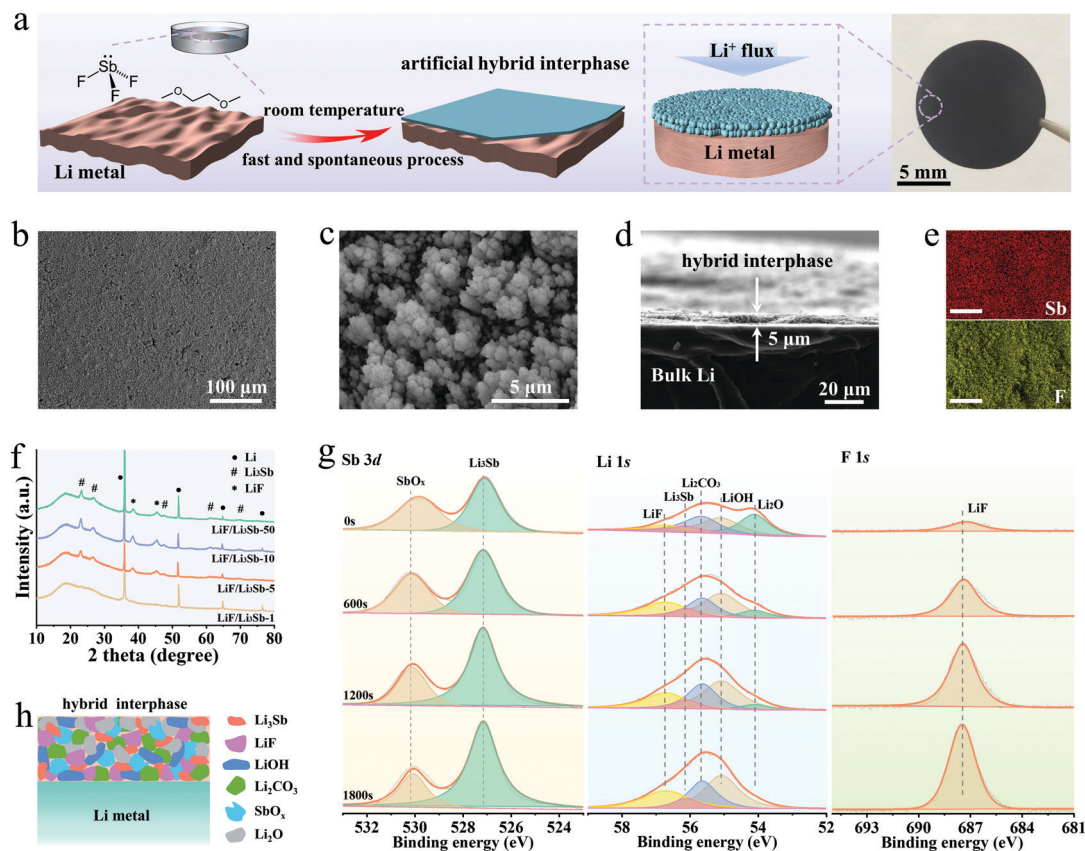*Energy Environ. Sci.*, 2021, **14**, 4115–4124 | **4117**

Fig. 2 Construction and characterization of the artificial hybrid interphase. (a) Schematic illustration of the hybrid interphase on Li foil and the optical image of the interphase (5 mM). (b and c) Top-view SEM images of the interphase (5 mM) covered on Li foil. (d) The cross-sectional SEM image of the interphase (5 mM). (e) The F and Sb elemental mappings of the interphase (5 mM). Scale bar: 50 μm. (f) XRD spectra of the interphase with different concentrations. To avoid direct contact of the electrode with air or moisture, all the samples were measured under the protection of kapton tape that has a wide diffraction peak at ~20°. (g) High-resolution XPS depth profiles of Sb 3d, Li 1s, and F 1s of LiF/Li₃Sb-5. (h) Schematic illustration of the interphase layer formed on the Li metal anode.

It can be confirmed that the upper surface region of the interphase is primarily composed of Li_3Sb, amorphous SbO_x and Li-based compounds (LiF, LiOH, Li_2CO_3, and Li_2O) (Fig. 2h). The characteristic XPS peak of Li_2O in the SEI layer almost completely disappears after 30 min of Ar^+ bombardment, revealing that Li_2O just exists in the upper surface. In the inner region, Li_3Sb and LiF are the major components.

The mechanical strength properties of the modified Li anode with the artificial hybrid LiF/Li₃Sb-5 interphase were investigated using AFM indentation (Fig. S14, ESI†). Compared with the bare Li (486 MPa), the higher mechanical strength (676 MPa) of hybrid LiF/Li₃Sb-5 endows the SEI layer with robust tolerance against the volume change during cycling, which is expected to protect the interfacial layer from the damage caused by Li dendrites. Furthermore, the electrolyte wettability of the LiF/Li₃Sb-5 layer was confirmed to present a negligible contact angle, which is favorable for the even distribution of the Li^+ flux and conductive to Li nucleation with a reduced nucleation barrier (Fig. S15 and Note S7, ESI†). The ionic conductivity and electronic resistivity of the LiF/Li₃Sb-5 layer were calculated to be 1.01×10^{-5} S cm^{-1} and 3.8×10^4 Ω cm, respectively (Fig. S16, S17 and Note S8, ESI†). Such high

electronic insulativity and ionic conductivity are expected to avoid the direct reduction of Li^+ at the artificial SEI/electrolyte interface and realize uniform Li deposition underneath the interphase layer.

Electrochemical performance of the modified Li anode

To validate the advantages of the LiF/Li₃Sb-5 modified Li anode, the electrochemical performances of the artificial hybrid interphase were investigated (Fig. 3). The nucleation overpotential of LiF/Li₃Sb-5 is 29 mV, much lower than that of bare Li (48 mV) at a rate of 2 mA cm^{-2} (2 mA h cm^{-2}) (Fig. 3a). The lower nucleation overpotential implies that the LiF/Li₃Sb-5 in the SEI allows fast Li^+ transfer across the SEI layer and promotes uniform Li nucleation. Thus, as displayed in Fig. 3b, the symmetric LiF/Li₃Sb-5 cell holds a stable cycling for over 600 h with a slight overpotential of 30 mV as the current density increases to 5 mA cm^{-2} with a high capacity of 5 mA h cm^{-2} while the bare Li suffers from a much larger overpotential (over 50 mV) and a sudden voltage drop after 84 h. In addition, the ESI measurements were carried out to compare the R_{ct} results of two symmetric cells at different states. As revealed by the EIS results (Fig. S18 and Table S7, ESI†), the R_{ct} of the cell with bare Li ever increases after 100 cycles due to the side reactions of Li
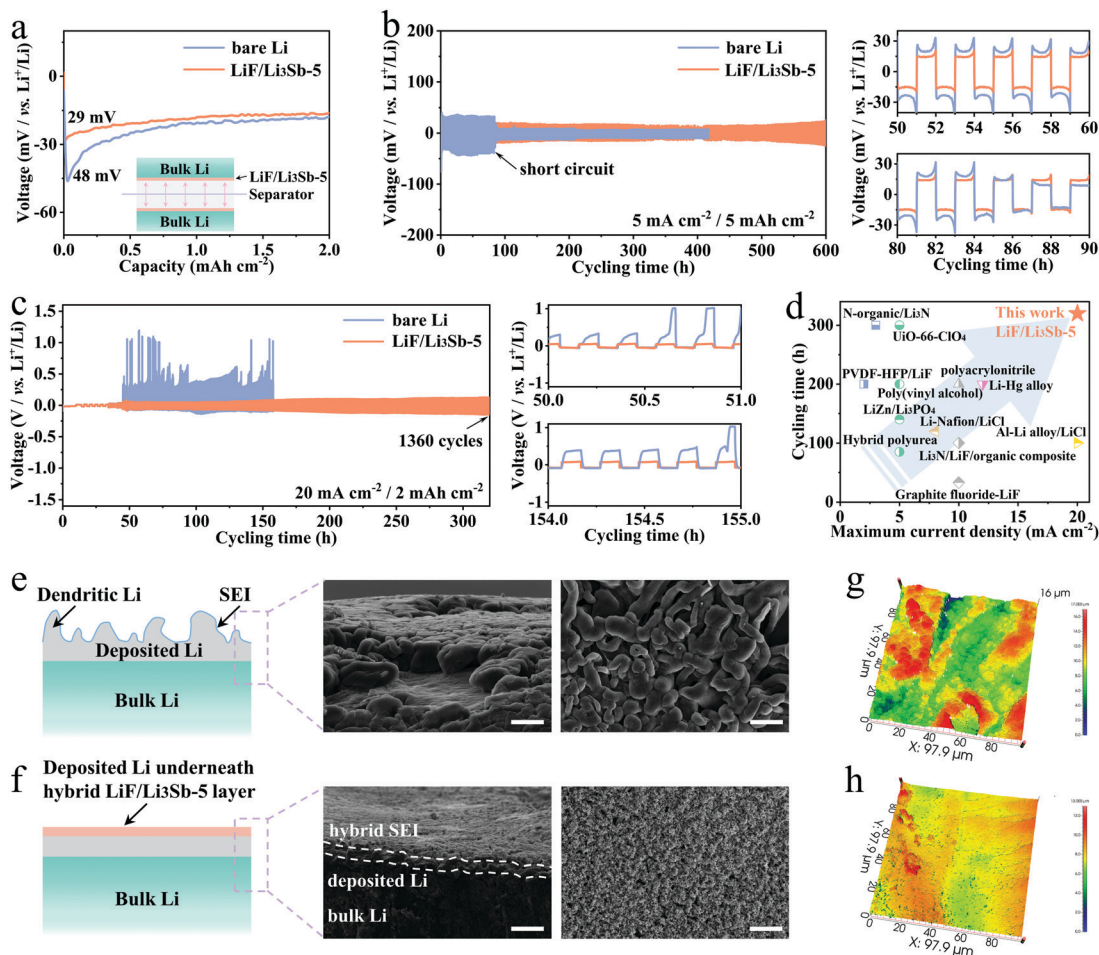
4118 | *Energy Environ. Sci.*, 2021, **14**, 4115–4124

This journal is © The Royal Society of Chemistry 2021

Fig. 3 Electrochemical stability of symmetric cells. (a) Nucleation overpotentials of bare Li and LiF/Li$_3$Sb-5 at a current density of 2 mA cm^{-2} with a capacity of 2 mA h cm^{-2}. (b) Voltage profiles and the corresponding discharge terminal voltages of symmetric cells with bare Li and LiF/Li$_3$Sb-5 at 5 mA cm^{-2} with a capacity of 5 mA h cm^{-2}. (c) Voltage profiles of symmetric cells with bare Li and LiF/Li$_3$Sb-5 at 20 mA cm^{-2} with a capacity of 2 mA h cm^{-2}. The applied current is gradually increased from 1, 3, 5, 10, and 15 mA (for 5 cycles of each protocol) to 20 mA for the long cycle. (d) Comparison of maximum current density and the corresponding cycle life of our LiF/Li$_3$Sb-5 with the representative SEI (detailed parameters are summarized in Table S8, ESI†). Schematic illustration and SEM images of Li deposition on (e) bare Li and (f) hybrid LiF/Li$_3$Sb-5 with a plating capacity 5 mA h cm^{-2} at a current density of 5 mA cm^{-2}. Scale bar: 50 μm. 3D optical profilometry images of (g) bare Li and (h) LiF/Li$_3$Sb-5 with a plating capacity of 5 mA h cm^{-2} at a current density of 5 mA cm^{-2}.

and the electrolyte, which indicates the high resistance of Li$^+$ diffusion through the interface. In contrast, the LiF/Li$_3$Sb-5 interphase layer is much more inert to the electrolyte because the resistance is much lower and remains almost constant even after cycling. Therefore, the high ionic conductivity in the hybrid interphase layer causes the low diffusion impedance of Li$^+$ and facilitates fast Li$^+$ diffusion and uniform Li deposition. Moreover, the high mechanical strength of the interphase layer can bear the volume fluctuations and provide good mechanical stability to suppress the growth of Li dendrites during cycling.[30] The superiority of the hybrid interphase layer is especially manifested at an ultra-high rate of up to 20 mA cm^{-2}. As shown in Fig. 3c, the symmetric cell with bare Li suffers from a serious voltage fluctuation, and it cannot sustain cycling under such high current density, since the Li$^+$ diffusion within the native SEI is limited. In sharp contrast, the symmetric LiF/Li$_3$Sb-5 cell can deliver excellent Li plating/stripping stability over

1360 cycles with a very low polarization of 100 mV, which is far superior to all reported results focusing on the modified SEI (Fig. 3d and Table S8, ESI†). These results demonstrate that the fast Li$^+$ diffusion kinetics of the hybrid interphase layer enables not only low overpotentials, but also flat and smooth cycling plateaus with a long lifespan at a high current density.

The role of the LiF/Li$_3$Sb-5 interphase layer in suppressing the dendrite growth was further validated by SEM and surface 3D topography. As shown in Fig. 3e and g, Li deposition on the bare Li anode exhibits nonuniform and uncontrolled growth, because the electrolyte-induced SEI layer is too fragile to tolerate the large volume variations during cycling, resulting in the penetration of Li dendrites and the breakage of the SEI. In contrast, the LiF/Li$_3$Sb-5 layer on the surface of the Li anode remains intact and uniform after plating and the dense Li is found to be deposited underneath the hybrid SEI layer (Fig. 3f and h). In addition, the

This journal is © The Royal Society of Chemistry 2021

Energy Environ. Sci., 2021, **14**, 4115–4124 | **4119**

investigation on the pure Li₃Sb and LiF SEI layer demonstrates the superiority of the hybrid SEI layer and the benefits of the fabrication using the low-cost SbF₃ precursor as the sole source rather than introducing another source of metal halides or fluorines (Fig. S19–S22 and Note S9, ESI†). Furthermore, the merits of the hybrid interphase layer to stabilize the Li anode were further validated in coin-type Li–S batteries (Fig. S23–S26 and Note S10, ESI†). These results further demonstrate the superiority of the modified Li anode in achieving fast interfacial ion transport at a high current density and suppressing the growth of Li dendrites.

Mechanism of Li⁺ transport in the artificial hybrid interphase

The role of the artificial hybrid interphase layer is critical to the superior electrochemical performance and Li deposition behavior. As shown in Fig. 4a, when the SEI exhibits a high electron-tunneling barrier while the Li⁺ diffusion rate in the SEI is fast
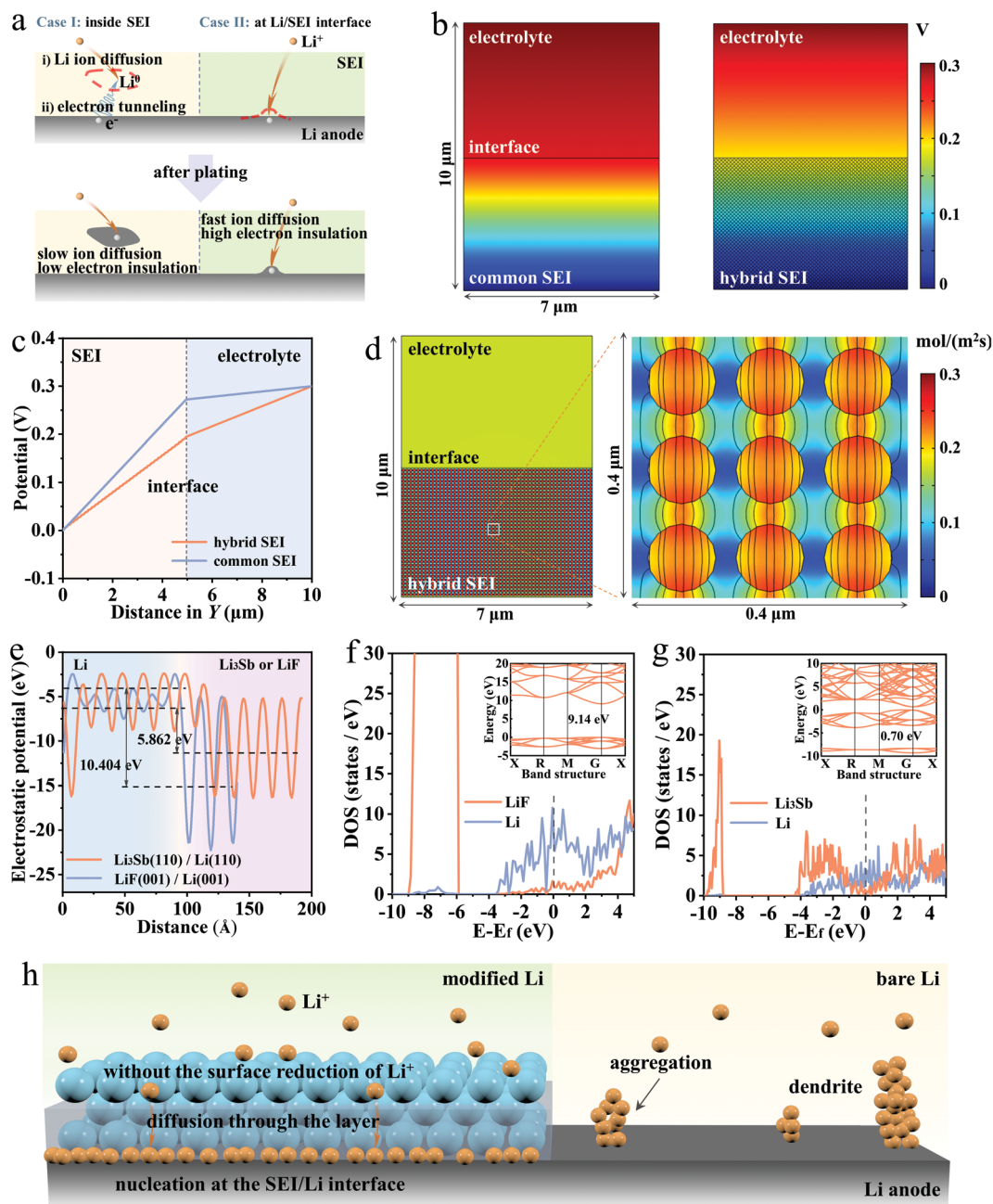

Fig. 4 Finite element simulation and mechanism understanding. (a) Proposed models of Li nucleation and growth mechanisms after Li plating. Finite element simulation of (b) potential and (c) potential distribution at the enlarged 10 μm × 7 μm scale for the common SEI and the hybrid SEI. (d) 1D cross-sectional Li⁺ flux distribution along the Y direction in the common SEI and the hybrid SEI. (e) Electrostatic potential profiles of Li₃Sb(110)/Li(110) and LiF(001)/Li(001) interfaces. Density of states (DOS) of (f) LiF(001)/Li(001) and (g) Li₃Sb(110)/Li(110) interfaces. The insets in (f) and (g) are the band structures of the LiF and Li₃Sb unit cell, respectively. (h) Schematic illustration of Li plating on LiF/Li₃Sb-5 modified Li and bare Li.

enough, Li deposition may occur at the SEI/Li interface. To better elaborate the Li deposition, the distribution of the electric potential field and Li^+ flux was simulated and visualized *via* the finite element simulation (FES). It can be observed from Fig. 4b that the hybrid SEI layer shows a more uniform electric field in the entire regions, compared with the common SEI. Fig. 4c presents a cross-sectional potential profile along the normal Y direction of the SEI. The electric potential gradient of the hybrid SEI is lower than that of the common SEI, which is beneficial for reducing the overpotential during cycling.[31] Moreover, the redistribution of the Li^+ flux after introducing the hybrid SEI was simulated in Fig. 4d. When the Li^+ diffusion coefficient of the hybrid SEI is much larger than that of the common SEI, the hybrid layer can redistribute the Li^+ flux and simultaneously provide faster Li^+ transport in the SEI.[32] As a result, the uniformly distributed Li^+ flux and electric field are conducive to promote dendrite-free Li deposition.[33]

Furthermore, the profiles of the planar-average electrostatic potential presented in Fig. 4e indicate that electrons in the Li metal at the interfaces possess higher energy (lower work function) than those in the SEI part, and thus tend to transfer from the Li bulk to the SEI side.[8] As a result, an electric field is built at the interface with the direction from Li pointing to the SEI side. The difference between the macro-average electrostatic potentials (approximately the Fermi level of the component on each side of the interface, represented by dashed lines in Fig. 4e) determines the strength of the internal electric-field. Obviously, the difference of 10.404 eV in LiF(001)/Li(001) is much larger than the value of 5.862 eV in the $Li_3Sb(110)/Li(110)$ interface, implying that electrons at the LiF(001)/Li(001) interface may meet the much higher barrier to tunnel into the SEI. Indeed, the inset in Fig. 4f shows that LiF is an insulator with a huge band gap of 9.14 eV, which can efficiently block electron tunneling in the LiF bulk. In contrast, Li_3Sb is a semiconductor with a small band gap of 0.70 eV (the inset in Fig. 4g), and the density of states (DOS) of Li_3Sb (Fig. 4g) is comparative to the feature of the Li metal of the interface around the Fermi level, indicating that the electrons may be capable of migrating from the Li anode to the inner part of Li_3Sb, and then combine with Li^+ to form Li metal nuclei inside the SEI. However, the DOS characteristic of LiF is rather weak compared to the DOS curve of the Li part of the interface. It is reasonable to believe that the inner part of LiF away from the interface would block the further tunneling of electrons inside the SEI and render the Li deposition at the interface.

To sum up, the reasonable Li deposition scenarios in the artificial hybrid interphase layer are established, as shown in Fig. 4h. The synergistic effect of the electronically insulating effect of LiF and the fast transport properties of Li_3Sb enables fast Li^+ diffusion across the interphase layer without reduction on its surface, by which the Li deposition occurs at the SEI/Li interface. The above processes may act in concert to realize dendrite-free Li growth underneath the hybrid SEI layer.

Validation in a practical pouch cell

The practical Li–S pouch cells with the artificial hybrid interphase are further employed for the actual visualization. As shown in

Fig. 5a and Note S11 (ESI†), a 0.4 A h-level pouch cell with a high areal sulfur loading (6 mg cm^{-2}) and a low E/S ratio (3 μl mg^{-1}) was fabricated to validate the effectiveness of the modified Li metal in practical operation. The configuration of the pouch cell is presented in Fig. S27 (ESI†), where multiple layers of S cathodes, separator and modified Li anodes are stacked together. Among the components, the LiF/Li_3Sb-5 modified anode can be easily produced on a large scale on a 100 μm-thickness commercial Li belt (100 × 250 mm) (Fig. S28, ESI†) and show excellent flexibility even under severe distortion (Fig. 5b).

The voltage curves of the 0.4 A h-level pouch cell in flat and bent states are presented in Fig. 5c. Two voltage plateaus located at ~2.3 V and 2.1 V (ΔE = 203 mV) can be clearly observed in both flat and bent states, indicating that our pouch cell exhibits negligible voltage hysteresis compared with coin cells. As a result, the pouch cell shows an excellent discharge specific capacity of 1034.19 mA h g^{-1} at a current density of 231.45 mA g^{-1}, corresponding to a practical energy density of 325.28 W h kg^{-1}. In addition, the cycling performance of the pouch cell was further tested at a current density of 231.45 mA g^{-1} in both flat and bent states at 180° (Fig. 5d). The pouch cell can still maintain a high capacity retention rate of 91.5% after 60 cycles and show little fluctuation even in the bent state within 50 cycles, supporting the effectiveness of the hybrid interphase even under practical conditions. The advantages of the LiF/Li_3Sb modified Li anode are further confirmed by comparing with the previously reported Li–S pouch cell, as shown in Fig. 5e and Table S9 (ESI†). It can be clearly observed that a significant advance is achieved in balancing cycle life and energy density, which is beneficial for next-generation high-energy-density electronic devices.[34]

Furthermore, the resultant pouch cell was applied for powering electronic devices to showcase its practical validation. As shown in Fig. 5f, light-emitting diodes (LEDs) with a clear caption of "UESTC" are successfully lighted up with the pouch cell. In addition, the pouch cell is connected to a mobile phone and an electric fan, which were charged and worked well, respectively, indicating that the modified Li anode endows the pouch cell with great potential as a power source for electronic devices.

Conclusions

In summary, the effectiveness of the hybrid LiF/Li_3Sb layer in stabilizing the Li anode at an ultrahigh rate and under practical conditions was convincingly demonstrated experimentally and theoretically. The LiF component with insulating behavior confines the tunneling electrons from the Li anode into the SEI while the excellent Li^+ transport properties of Li_3Sb provide an ion channel for fast Li^+ diffusion across the interphase layer, which act in concert to achieve dendrite-free Li deposition underneath the artificial hybrid interphase. In addition, the high interfacial mechanical strength and good electrochemical stability of the interphase inhibit the Li dendrite growth during repeated cycling. Outstanding electrochemical performances were achieved in the symmetric LiF/Li_3Sb cell demonstrating

This journal is © The Royal Society of Chemistry 2021

Energy Environ. Sci., 2021, **14**, 4115–4124 | **4121**
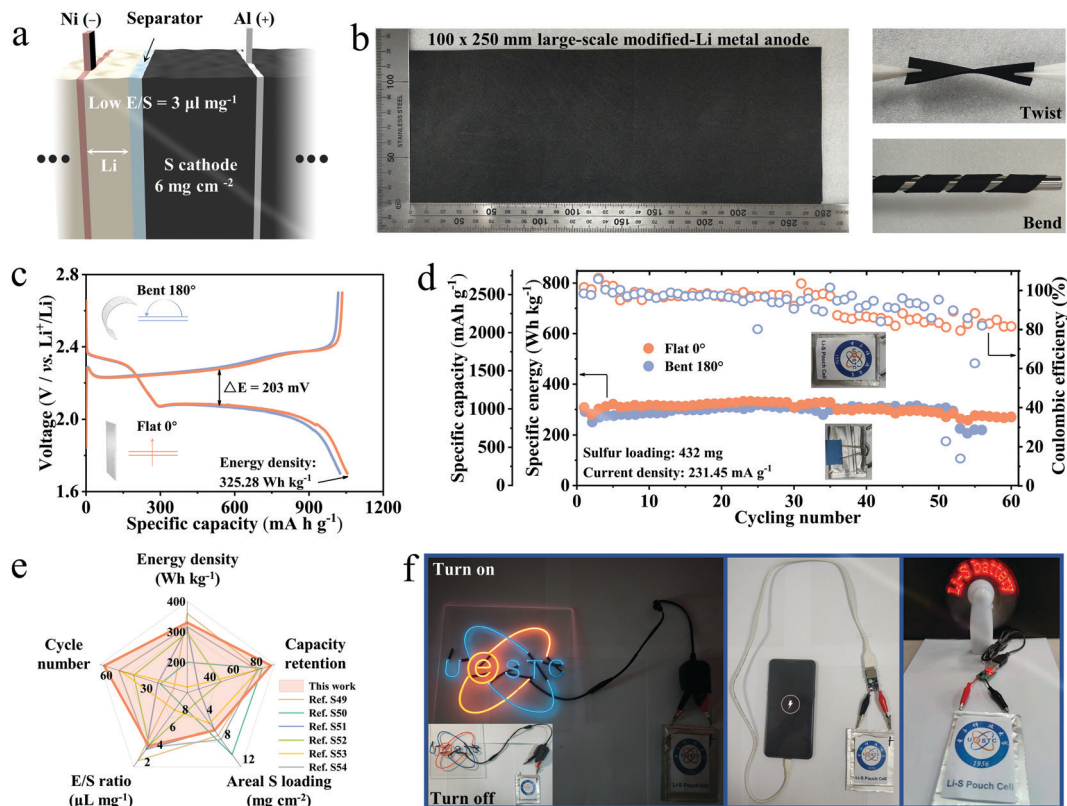
Fig. 5 Electrochemical performance of practical pouch cells. (a) Schematic illustration of a pouch cell with a high-loading cathode, lean electrolyte, and limited amount of the Li anode. (b) Digital photographs of large-scale LiF/Li$_3$Sb-5 foil and its flexibility even under severe distortion (twist and bend). (c) Charge/discharge curves and (d) cycling performance of the pouch cell in flat and bent states at 231.45 mA g^{-1}. (e) Radar plots for the performance comparison of this work and related references on the vital parameters of practical Li–S pouch cells. (f) Digital photographs of the pouch cell lighting up LEDs and powering a mobile phone and an electric fan.

long-term Li plating/stripping stability (1360 cycles) with a low voltage hysteresis (100 mV) at an ultrahigh rate of 20 mA cm^{-2}. A 0.4 A h-level Li–S pouch cell with a high sulfur loading (6 mg cm^{-2}) and a low E/S ratio (3 μl mg^{-1}) has been successfully demonstrated to exhibit a high practical specific energy of 325.28 W h kg^{-1} and a stable life of 60 cycles with a capacity retention of 91.5%. This work elucidates the role of an artificial SEI in stabilizing Li metal anodes, providing an alternative approach for the development of other metal anodes such as Na and Zn anodes.

Experimental

Electrode preparation

The bare Li foil (99.9%, 500 μm) was first polished to remove surface contaminants by using a nylon brush in the aprotic solvent of tetrahydrofuran (THF, inhibitor-free; Sigma-Aldrich) and dried in a glove box before use. To construct a fluorinated lithiophilic interphase on the Li surface, different concentrations (x mM, x = 1, 5, 10, and 50) of antimony trifluoride (SbF$_3$, 99.8%; Sigma-Aldrich) were dispersed in the dimethyl ether (DME) aprotic solvent by vigorously stirring for several hours. After being soaked for 180 s, the surface color of the Li metal became black. Then, the treated Li was rinsed using DME and dried at

60 °C under Ar overnight, and finally the fluorinated lithiophilic interphase on the Li electrode was obtained. The interphase layer with different concentrations of SbF$_3$ is represented as LiF/Li$_3$Sb-x (x = 1, 5, 10, and 50).

Material characterization

XRD was carried out using an Ultima IV diffractometer (Rigaku) with Cu Kα radiation (λ = 1.5406 Å). The morphologies and mappings were obtained using FE-SEM (Nova NANOSEI 450). XPS was investigated using a Thermo Scientific K-Alpha$^+$ system with monochromatic Al Kα radiation (1486.6 eV). TOF-SIMS was measured on a PHI nanoTOF II. Raman spectra were measured using a Renishaw 200 system (532 nm). The 3D topography and roughness were studied using an optical 3D surface profiler (SuperView W1). The mechanical properties were investigated on an AFM (Bruker Dimension ICON). The contact angle was obtained on an OCA20 system.

Electrochemical measurements

The coin cells (CR-2032) were used to evaluate the electrochemical performance. The symmetric cells with bare Li and modified Li anodes were assembled in the Ar-filled glove box. The electrolyte is 1 M bis(trifluoromethane) sulfonimide Li salt (LiTFSI) with 2% LiNO$_3$ dissolved in a mixture of 1,3-dioxolane (DOL) and dimethyl

ether (DME) (1:1, v/v). The separator is Celgard 2400 poly-propylene (25 μm). For Li–S battery tests, the cathode was obtained by coating the mixture of sulfur, acetylene black and polyvinylidene fluoride (7:2:1, in N-methylpyrrolidone) onto the carbon coated aluminum foil. The sulfur loading in the cathode is 2 mg cm^{-2}. The used volume of the electrolyte is controlled to be ∼40 μl in each cell. The galvanostatic measurements of the Li–S battery were conducted on LAND CT2001A systems. Cyclic voltammetry (CV), linear sweep voltammetry (LSV), and electrochemical impedance spectroscopy (EIS) were performed using the CHI660E electrochemical workstation. The EIS measurement was conducted with a 5 mV amplitude AC signal with a frequency of 100 kHz–0.1 Hz.

Computational methods

The spin polarized first-principles calculations based on density functional theory (DFT) were conducted using the Vienna Ab initio Simulation Package (VASP)[35–37] for the theoretical study. The generalized gradient approximation (GGA) with the Perdew–Burke–Emzerhof (PBE) functional[38,39] was used to describe the exchange correlation energy. Projector Augmented Wave (PAW)[40] methods were employed for the pseudo-potentials. The energy cutoff for the plane wave basis was set as 450 eV and the convergence criterion of geometry relaxation was 0.02 eV Å^{-1} in force. The Brillouin zones (BZ) were sampled by K point grids of $2\pi \times 0.02$ Å^{-1}. To build the model for investigation of Li$^+$ adsorption and diffusion on the surfaces, a vacuum of 15 Å was added along the direction normal to the atomic slab. Transition states of Li$^+$ diffusion and kinetic barriers were determined by the CI-NEB method[41] implemented in the VASP code.

Finite element simulation

The COMSOL Multiphysics 5.4 was used for the transport of diluted species and electrostatic field simulations in this work.[42] The steady-state plating of the LiF/Li$_3$Sb-5 and original SEI shrouded electrode was conducted in 7×10 μm^2 2D areas, respectively. Faraday's law and current density were coupled at the electrode interface. The electrolyte conductivity is 10^{-2} S m^{-1}. The lithium ion concentration is 1 M and its diffusion coefficient in the electrolyte, common SEI, and hybrid SEI is 1×10^{-5}, 1×10^{-9} and 1×10^{-4} S m^{-1}, respectively. The plating voltage difference between the two ends of the model was set as 0.3 V.

Author contributions

J. X. and X. W. conceived and designed this work. A. H. and W. C. did the experiments and wrote the paper. B. L. performed the first-principles calculations. D. X. performed the finite element simulation. Y. H., T. L., L. X., and Y. L. measured the electrochemical performance. H. W., H. S., Y. Y., J. L., C. Z., and J. Z. conducted characterization and analysis. All authors participated in analysis of the experimental data and discussions of the results, as well as in editing the manuscript.

Conflicts of interest

There are no conflicts to declare.

Acknowledgements

References

1 F. Duffner, N. Kronemeyer, J. Tübke, J. Leker, M. Winter and R. Schmuch, *Nat. Energy*, 2021, **6**, 123–134.

2 M. Balaish, J. C. Gonzalez-Rosillo, K. J. Kim, Y. Zhu, Z. D. Hood and J. L. M. Rupp, *Nat. Energy*, 2021, **6**, 227–239.

3 J. Holoubek, H. Liu, Z. Wu, Y. Yin, X. Xing, G. Cai, S. Yu, H. Zhou, T. A. Pascal, Z. Chen and P. Liu, *Nat. Energy*, 2021, **6**, 303–313.

4 Y. Han, B. Liu, Z. Xiao, W. Zhang, X. Wang, G. Pan, Y. Xia, X. Xia and J. Tu, *InfoMat*, 2021, **3**, 155–174.

5 A. Hu, M. Zhou, T. Lei, Y. Hu, X. Du, C. Gong, C. Shu, J. Long, J. Zhu, W. Chen, X. Wang and J. Xiong, *Adv. Energy Mater.*, 2020, **10**, 2002180.

6 J. Xiao, *Science*, 2019, **366**, 426–427.

7 B. Tang, H. Wu, X. Du, X. Cheng, X. Liu, Z. Yu, J. Yang, M. Zhang, J. Zhang and G. Cui, *Small*, 2020, **16**, 1905737.

8 Z. Liu, Y. Qi, Y. X. Lin, L. Chen, P. Lu and L. Q. Chen, *J. Electrochem. Soc.*, 2016, **163**, A592–A598.

9 H. Wu, H. Jia, C. Wang, J.-G. Zhang and W. Xu, *Adv. Energy Mater.*, 2021, **11**, 2003092.

10 Z. Wei, Y. Ren, J. Sokolowski, X. Zhu and G. Wu, *InfoMat*, 2020, **2**, 483–508.

11 X. Ji, S. Hou, P. Wang, X. He, N. Piao, J. Chen, X. Fan and C. Wang, *Adv. Mater.*, 2020, **32**, 2002741.

12 S. Liu, X. Ji, J. Yue, S. Hou, P. Wang, C. Cui, J. Chen, B. Shao, J. Li, F. Han, J. Tu and C. Wang, *J. Am. Chem. Soc.*, 2020, **142**, 2438–2447.

13 Z. Hu, S. Zhang, S. Dong, W. Li, H. Li, G. Cui and L. Chen, *Chem. Mater.*, 2017, **29**, 4682–4689.

14 S. K. Heiskanen, J. Kim and B. L. Lucht, *Joule*, 2019, **3**, 2322–2333.

15 Y. C. Chen, C. Y. Ouyang, L. J. Song and Z. L. Sun, *J. Phys. Chem. C*, 2011, **115**, 7044–7049.

16 J. Ko and Y. S. Yoon, *Ceram. Int.*, 2019, **45**, 30–49.

17 X.-B. Cheng, C. Yan, X.-Q. Zhang, H. Liu and Q. Zhang, *ACS Energy Lett.*, 2018, **3**, 1564–1570.

18 Y. Gao, Z. Yan, J. L. Gray, X. He, D. Wang, T. Chen, Q. Huang, Y. C. Li, H. Wang, S. H. Kim, T. E. Mallouk and D. Wang, *Nat. Mater.*, 2019, **18**, 384–389.

19 G. Li, Y. Gao, X. He, Q. Huang, S. Chen, S. H. Kim and D. Wang, *Nat. Commun.*, 2017, **8**, 850.

This journal is © The Royal Society of Chemistry 2021

Energy Environ. Sci., 2021, **14**, 4115–4124 | **4123**

20 X. Shen, R. Zhang, X. Chen, X.-B. Cheng, X. Li and Q. Zhang, *Adv. Energy Mater.*, 2020, **10**, 1903645.

21 X. Cao, X. Ren, L. Zou, M. H. Engelhard, W. Huang, H. Wang, B. E. Matthews, H. Lee, C. Niu, B. W. Arey, Y. Cui, C. Wang, J. Xiao, J. Liu, W. Xu and J.-G. Zhang, *Nat. Energy*, 2019, **4**, 796–805.

22 F. A. Soto, Y. Ma, J. M. Martinez de la Hoz, J. M. Seminario and P. B. Balbuena, *Chem. Mater.*, 2015, **27**, 7990–8000.

23 R. F. Bader, *Chem. Rev.*, 1991, **91**, 893–928.

24 Y. X. Ren, L. Zeng, H. R. Jiang, W. Q. Ruan, Q. Chen and T. S. Zhao, *Nat. Commun.*, 2019, **10**, 3249.

25 J. Zhu, P. Li, X. Chen, D. Legut, Y. Fan, R. Zhang, Y. Lu, X. Cheng and Q. Zhang, *Energy Storage Mater.*, 2019, **16**, 426–433.

26 X. Liang, Q. Pang, I. R. Kochetkov, M. S. Sempere, H. Huang, X. Sun and L. F. Nazar, *Nat. Energy*, 2017, **2**, 17119.

27 M. D. Tikekar, S. Choudhury, Z. Tu and L. A. Archer, *Nat. Energy*, 2016, **1**, 16114.

28 R. Xu, X.-B. Cheng, C. Yan, X.-Q. Zhang, Y. Xiao, C.-Z. Zhao, J.-Q. Huang and Q. Zhang, *Matter*, 2019, **1**, 317–344.

29 R. Pathak, K. Chen, A. Gurung, K. M. Reza, B. Bahrami, J. Pokharel, A. Baniya, W. He, F. Wu, Y. Zhou, K. Xu and Q. Qiao, *Nat. Commun.*, 2020, **11**, 93.

30 Y.-X. Yao, X.-Q. Zhang, B.-Q. Li, C. Yan, P.-Y. Chen, J.-Q. Huang and Q. Zhang, *InfoMat*, 2020, **2**, 379–388.

31 L. Chen, H. W. Zhang, L. Y. Liang, Z. Liu, Y. Qi, P. Lu, J. Chen and L.-Q. Chen, *J. Power Sources*, 2015, **300**, 376–385.

32 Y. Zhou, X. Zhang, Y. Ding, J. Bae, X. Guo, Y. Zhao and G. Yu, *Adv. Mater.*, 2020, **32**, 2003920.

33 G. Li, Z. Liu, Q. Huang, Y. Gao, M. Regula, D. Wang, L.-Q. Chen and D. Wang, *Nat. Energy*, 2018, **3**, 1076–1083.

34 Y. Hu, W. Chen, T. Lei, Y. Jiao, J. Huang, A. Hu, C. Gong, C. Yan, X. Wang and J. Xiong, *Adv. Energy Mater.*, 2020, **10**, 2000082.

35 G. Kresse and J. Furthmüller, *Phys. Rev. B: Condens. Matter Mater. Phys.*, 1996, **54**, 11169–11186.

36 G. Kresse and J. Furthmüller, *Comput. Mater. Sci.*, 1996, **6**, 15–50.

37 G. Kresse and J. Hafner, *Phys. Rev. B: Condens. Matter Mater. Phys.*, 1994, **49**, 14251.

38 J. P. Perdew, J. A. Chevary, S. H. Vosko, K. A. Jackson, M. R. Pederson, D. J. Singh and C. Fiolhais, *Phys. Rev. B: Condens. Matter Mater. Phys.*, 1992, **46**, 6671.

39 A. Hu, W. Lv, T. Lei, W. Chen, Y. Hu, C. Shu, X. Wang, L. Xue, J. Huang, X. Du, H. Wang, K. Tang, C. Gong, J. Zhu, W. He, J. Long and J. Xiong, *ACS Nano*, 2020, **14**, 3490–3499.

40 P. E. Blöchl, *Phys. Rev. B: Condens. Matter Mater. Phys.*, 1994, **50**, 17953.

41 G. Henkelman, B. P. Uberuaga and H. Jónsson, *J. Chem. Phys.*, 2000, **113**, 9901–9904.

42 W. Chen, Y. Hu, W. Lv, T. Lei, X. Wang, Z. Li, M. Zhang, J. Huang, X. Du, Y. Yan, W. He, C. Liu, M. Liao, W. Zhang, J. Xiong and C. Yan, *Nat. Commun.*, 2019, **10**, 4973.

4124 | *Energy Environ. Sci.*, 2021, **14**, 4115–4124

This journal is © The Royal Society of Chemistry 2021